Optimization of Frequency Measurements for Quantum Magnetometers

Evgeny V. Karshakov, and Andrey K. Volkovitsky

***Abstract*— Most known quantum magnetometers have a periodic signal at the output. By measuring its frequency, it is possible to estimate the value of the magnetic field induction. In many applications, such as aeromagnetic measurements, one needs to increase the sampling rate, but this also increases the measurement error. The article describes two algorithms for obtaining frequency measurements depending on the characteristics of the equipment. One averages the periods over one sample, the other averages the frequency over the same time gate. It is shown that the frequency estimate can perform better than the period estimate. As an example, a ^{133}Cs optically pumped sensor and a reference frequency of 1 GHz at a sampling rate of 1 kHz were considered. In the case of an ideal input signal, the frequency estimation error corresponds to $\pm$0.074 nT around some regular values every 9 nT, and the period estimation error corresponds to $\pm$0.049 nT every 0.05 nT. In the case of signal noise of 0.5 pT/$\sqrt{\text{Hz}}$, the frequency estimation error corresponds to $\pm$0.058 nT, and for the period estimation error it is $\pm$0.278 nT under the same conditions. The paper also describes how to use a satellite navigation system as a time reference to ensure frequency estimation accuracy. In this case the uncertainty can be as low as $2{\cdot}10^{-8}$, or about 1 pT in terms of magnetic field induction. All the ideas are illustrated by experiments. It is shown that for this frequency counter a sampling rate of up to 1 kHz can be used with the considered sensors.**

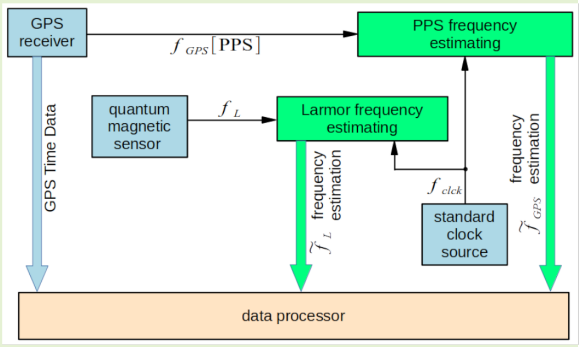

***Index Terms*— frequency measurement, proton-precession magnetometer, optically pumped magnetometer, Larmor precession**

I. Introduction

GEOMAGNETIC field measurement can be considered one of the main geophysical methods for studying the near-surface structure of the Earth since the middle of the 19$^{\text{th}}$ century [1]. At present, airborne, shipborne and ground magnetic surveys are widely used for various purposes. In our opinion, airborne survey is the most difficult task, and we can give at least two reasons. First, trying to study a weak anomaly of the geomagnetic field, it is better to measure it as close as possible to the source of the field. Going higher from the Earth's surface, we need to have a more sensitive instrument. Secondly, aircrafts move at a high speed. Those used for airborne magnetics fly at 50–100 meters per second, such as the Cessna-208. So the sample rate must be high enough. Moreover, aircraft interference can have a big impact and have a very high frequency. Leliak's well-known model of aircraft interference effects accounts for permanent magnetism from ferromagnetic parts in the aircraft, induced magnetism created by the Earth's magnetic field in soft-iron or paramagnetic parts, and Eddy-current magnetic fields created from electric currents produced on conducting paths of the airframe [2], [3]. But it is also necessary to exclude influence at higher frequencies. For example, the electromagnetic field of interference created by vibration and rotation of the rotor blades in the case of a helicopter platform [4]. And in some cases, an electromagnetic (EM) system is used together with the on-board magnetic system. Such systems generate an alternating magnetic field of large magnitude [5]. This means that the sample rate must be even higher than it is necessary for the survey itself.

This work is organized as follows. After a brief history of magnetic measurements, we will describe the most appropriate method for measuring frequency in relation to airborne magnetics. We then explain how to provide accurate frequency measurements using the Global Navigation Satellite System (GNSS). Next, we proceed to the analysis of the frequency estimation algorithm to obtain the best solution. Signal noise influence is also analyzed. Finally, we present some experimental results obtained with quantum magnetometers.

II. Historical Overview

The history of airborne magnetics began in 1936 in the USSR [6], and since then several generations of airborne magnetic sensors have been introduced. Starting with terrestrial

29/03/2024

The authors are with the Dynamic Control Systems Laboratory of the Institute of Control Sciences of Russian Academy of Sciences, Moscow, Russia (e-mail: karshakov@ipu.ru).

inductors and fluxgate sensors, the first proton magnetometer was introduced in the second half of the 20th century [1]. Its airborne version was launched in 1964 in Canada [7].

A. Proton-Precession Magnetometers

In a proton precession magnetometer (PPM), the idea is to measure the frequency of the free precession of polarized protons (hydrogen nuclei). After the polarizing field is removed, the proton precesses around the magnetic field vector like a heavy gyroscope in a gravitational field. The precession angular velocity is known as *Larmor Precession Frequency*, which is related to the magnetic field as follows [8], [9]:

$$f_p = \gamma_p \cdot B_0, \tag{1}$$

where B_0 is the magnitude of the magnetic induction vector measured in nT, f_p is the precession frequency in Hz, $\gamma_p = 1/23.487...$ nT^{-1}·s^{-1} is the gyromagnetic ratio of protons. The exact value of γ_p depends on the specific substance used in the sensor. In any case, for the geomagnetic field, the frequency range is 0.8–4.3 kHz, approximately 20,000–100,000 nT.

The quality of the signal depends on the volume of the sensor. The larger the volume, the more stable the signal is, but the sensor becomes less tolerant to the field gradient, which is a serious problem in the case of airborne applications. Due to the weak signal of the airborne sensors, they had a sensitivity of about 0.1–1 nT at a sampling rate of 1–3 times per second. Note that polarization and measurement in PPM are performed sequentially, one after the other.

In 1980s an Overhauser PPM was developed [7]. It used a special substance to get much more stable signal. As a result, in Overhauser magnetometer the signal can be measured simultaneously with polarization. Thus, such sensors have a sensitivity of 0.01 nT at a 1–10 Hz sampling rate. Nevertheless, they did not gain much popularity, since optically pumped magnetometers (OPMs) appeared around the same time.

B. Optically Pumped Magnetometers

For the manufacture of OPM, a cell filled with vapor from elements with suitable spaced magnetic energy sublevels is needed. The distance between the sublevels is a function of an external static magnetic field, which is known as the Zeeman effect. In modern practice, cesium, potassium or rubidium are most often found. Sodium and helium are also mentioned in [1]. A beam of light with circular polarization is used to "pump" the atoms in the cell. The beam is often generated by a lamp with the same element as the light source. When all atoms are already excited, the cell becomes transparent to light, and the photosensitive detector registers the maximum current. Now, beacause of the coil around the cell which generates radio-frequency (RF) waves, the cell becomes opaque again. But the energy or frequency of the wave must correspond exactly to the energy difference between the sublevels, which, according to Zeeman, in the first approximation is proportional to the magnitude of the magnetic field. Thus, as for PPM (1), there is a relationship between the magnetic induction and the Larmor frequency:

$$f_e = \gamma_e \cdot B_0, \tag{2}$$

where the gyromagnetic ratio γ_e depends on the element e.

For example, ^{133}Cs (let's denote it by $e = Cs$) has $\gamma_{Cs} = 3.498577$ nT^{-1}·s^{-1} [10]. This means that for the geomagnetic field the frequency range for f_{Cs} is 70–350 kHz. If ^{85}Rb is used ($e = Rb85$), then $\gamma_{Rb85} = 4.66743$ nT^{-1}·s^{-1} [11], [12]. The f_{Rb85} range is slightly shifted in relation to the previous one — 90–470 kHz. Three other isotopes ^{87}Rb, ^{39}K and ^{41}K have very close gyromagnetic ratios: $\gamma_{Rb87} = 6.99583$ nT.$^{-1}$·s^{-1}, $\gamma_{K39} = 7.00466$ nT^{-1}·s^{-1} and $\gamma_{K41} = 7.00533$ nT^{-1}·s^{-1} [12]. Thus, the frequency range for these elements is 140-700 kHz. In any case, the frequencies are about two orders higher than for PPM, which means that the sampling rate can theoretically be increased to 1 kHz and even more.

Currently, there are two most common types of such sensors. The quantum M_X sensor measures the frequency of forced oscillations of the transverse component of the total atomic magnetic moment [13] (relative to the external magnetic field). M_Z OPM measures the component parallel to the external magnetic field. The M_Z sensors are very accurate, and the M_X devices are characterized by a fast response [14]. The main reason for the high speed of the M_X sensor is that it does not use frequency modulation of RF field to find the resonance line center. It can be made self-oscillating when the photocurrent amplifier is directly connected to the RF field coil via a feedback loop [13]. In the case of the M_Z magnetometer, its operation speed and sensitivity are related to the width of the RF field resonance line. Typically, to ensure high sensitivity during the measurement of the center of a symmetric M_Z resonance, the line width is limited to an order of tens of hertz, which limits its bandwidth by the same value.

Self-oscillating ^{133}Cs M_X OPM sensors have gained great popularity in recent decades and have already proven their effectiveness in airborne geophysics for both total field measurements and gradiometry [15]. Such sensors are also effectively used for autonomous aircraft navigation [16]. We can list Canadian Scintrex [17] sensors, US Geometrics [18] sensors, Russian Radar-mms [19] sensors. In this study we will consider only this type of sensors.

III. Frequency Measurement Method

Having carried out the analysis, we can state that there are three main approaches to measuring the Larmor frequency.

- The period of the measured signal is compared with the period of the internal clock generating some fixed standard frequency [10], [20], [21]. The main problem with this method is that the result depends on the quality of the reference clock. It must be more stable than the magnetic sensor signal and its frequency must be high enough for the desired sample rate. The method will be described in the following chapters.
- The internally generated harmonic signal is compared to the Larmor signal and fine tuned to have the same

frequency and phase [13]. This synthetic signal is well known, so if we use its frequency as the output, it will not contain any noise. The problem is that the tuning algorithm has a limited bandwidth and it is difficult for it to track very fast field changes. This feature makes this approach less suitable for airborne applications.

- The Larmor signal after analog-to-digital conversion (ADC) is analyzed in the frequency domain to find the maximum. This idea has been applied to Overhauser sensors [22]. The method utilizes high precision ADC to obtain the discrete sequence of precession signal, and the discrete sequence is processed by Fast Fourier Transform (FFT) algorithm to determine the rough frequency of precession signal. Obviously, the higher the sampling rate, or the shorter the measurement time, the less detailed spectrum we get after applying the FFT. The spectrum zoom algorithm according to [22] interpolates the spectrum and provides 10^{-6} accuracy at 4096 points or more. In another paper, less optimistic numbers are given, about 10^{-3} for 1024 points [23]. The same hesitation is shown in [21]. Thus, the method is still under study.

Thus, we will follow the first approach. We will start with the counting algorithm itself, assuming that the signal noise is neglectable. We then look at how signal noise affects the estimate.

The main idea is shown in Fig. 1 and is used in many modern magnetometers, both OPM [10], [20] and PPM [24], [25]. The frequency meter must have an internal clock that generates pulses of high and stable frequency f_{clck}, they are shown in the lower graph. By dividing it, we can get fixed gates with a period of T_f (upper graph in Fig. 1). In each gate, it is necessary to count the number of periods of the measured signal.

The measured Larmor signal is a sine wave. By controlling when it crosses zero, the frequency meter generates pulses for counting (plot *measured signal* in Fig. 1).To eliminate the influence of noise near zero, the comparison level is different for an increasing and decreasing signal, see Schmitt trigger [26]. The processor counts the number of Larmor periods N in the current gate and the number of standard clock periods n, or period $T = n/f_{clck}$. As can be seen in Fig. 1, the real gate period T almost always differs from the fixed period T_f by the difference between τ and τ_1, as shown in the top two charts:

$$T = T_f + \tau - \tau_1. \tag{3}$$

An estimate of the Larmor period $\tilde{T}_{Lp}$ and the corresponding frequency $\tilde{f}_{Lp}$ can be easily obtained from the quantities described above:

$$\tilde{T}_{Lp} = \frac{T}{N}, \quad \tilde{f}_{Lp} = \frac{N}{T}. \tag{4}$$

Note that the value of T can be considered as the sum of all measured periods T_j, $j = 1, \ldots, N$ covered by the current gate. So we can rewrite (4) as

$$\tilde{T}_{Lp} = \frac{\sum_{j=1}^{N} T_j}{N}, \quad \tilde{f}_{Lp} = \frac{N}{\sum_{j=1}^{N} T_j}. \tag{5}$$

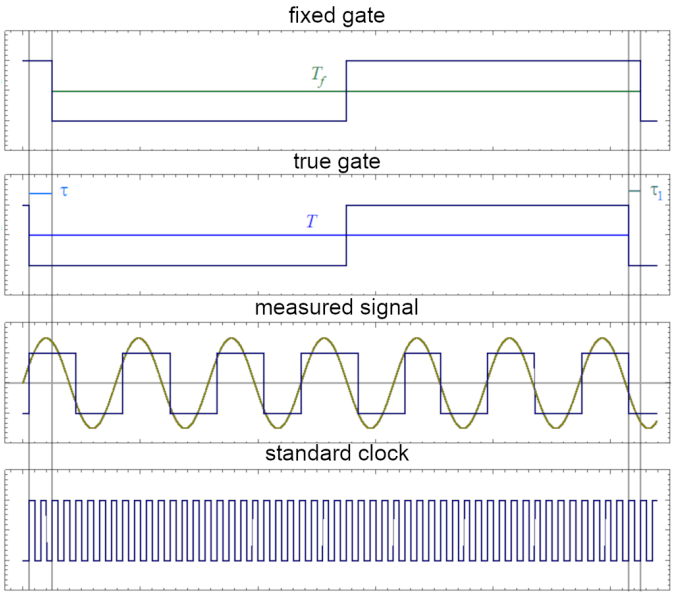

Fig. 1. Sequence diagram of the frequency measurement method. (standard clock) An internally generated reference clock used by the processor to sample Larmor signal zero crossings and for a counter. (measured signal) An idealized Larmor signal and a corresponding logic signal to measure its period. (true gate) Signal synchronized with the Larmor wave, $\boldsymbol{\tau}$ is the time remaining from the previous gate between the last zero crossing in the previous gate and the start of the current gate, $\boldsymbol{\tau_1}$ is the time between the last zero crossing in the current gate and the start of the next gate, $\boldsymbol{T}$ is the length of the sampled Larmore waves in the current gate, measured by internal clock. (fixed gate) A field sampling strobe that determines the sampling rate of field measurements, $\boldsymbol{T_f}$ is the measurements period.

Thus, $\tilde{T}_{Lp}$ is the average period value during the sampling gate. So, the result can be considered as applying of the Least squares method (LSM) to estimate the period.

The relative error in (4) obviously depends on the frequency of the reference clock f_{clck} and the sample rate of the Larmor signal measurements. To estimate the error, we can assume that the true sample gate is equal to the fixed sample gate at the frequency f_s, so the error is [10]:

$$\delta f_{Lp} = \frac{\Delta f_L}{f_L} \in \left(-\frac{f_s}{f_{clck}}, \frac{f_s}{f_{clck}} \right). \tag{6}$$

In the following sections, we will discuss two ways to ensure accuracy of frequency measurements. First, we use GNSS measurements to stabilize the reference clock. And then we analyze the possibility of using information about the duration of each of the Larmor periods covered by the current sampling gate.

IV. Satellite Atomic Clock

Modern airborne surveys are always carried out using some kind of GNSS receiver in order to know exactly the coordinates of the measurements. But it is well known that the GNSS solution evaluates not only the position, but also the time [27]. Since the coordinates and the clock error are estimated from the same set of measurements of the propagation time of electromagnetic signals, the error in units of time remains the same for the two quantities. Given the root mean square (RMS)

positioning error $\sigma_p = 5$ m [27], it is easy to calculate the time error $\sigma_t = \sigma_p/c \approx 17$ ns, c is the speed of light. GNSS receivers are capable of outputting a signal synchronized with the satellites' atomic clocks. It's called *Pulse Per Second* (PPS) and is typically generated at 1 Hz.

The PPS signal can be used in various applications. For example, to synchronize different devices [28]. Since all receivers have the same RMS σ_t, its value determines the synchronization accuracy.

Let's use the standard clock of the frequency meter to measure the duration of 1 s in the PPS signal. In this case, the resulting counter value is an estimate of the true value of the reference clock frequency $\tilde{f}_{clck} \in (f_{clck} - 1, f_{clck} + 1)$. Now, using it to calculate $T = n/\tilde{f}_{clck}$ in (4), we can be sure that the relative RMS error of the frequency estimate is within the following limits:

$$\delta \in (-1.7 \cdot 10^{-8}, 1.7 \cdot 10^{-8}). \tag{7}$$

Suppose in (6) the sample frequency $f_s \gg 1$ Hz. Then we can neglect the ± 1 error (7) of PPS signal measurements.

Thus, if we have a not very accurate (and not very expensive) internal clock, we can use PPS to reduce the error to δ in (7). Changes in the constellation of satellites may result in an outlier, but it will be of the same magnitude. In the case of OPM measurements, this corresponds to a value of about 1 pT. Unfortunately, it slightly exceeds the sensitivity of OPM [17]–[19]. Even though the sensors are accurate to a few hundred pT, there will be a step in the output. For this reason, we apply a filter to eliminate outliers.

Fig. 2 shows the results of measuring the PPS signal. This experiment was conducted using the GlobalSat SiRF-Star III ET-332 receiver. The top graph shows the number of visible satellites. The system has just been turned on. Initially, the GNSS receiver does not see any satellites. Around 17:35:50 it starts processing the signals, but three satellites are not enough to get a four-dimensional solution containing time and position. The solution to the navigation problem appears only after 17:36:00, when the fourth satellite comes into view.

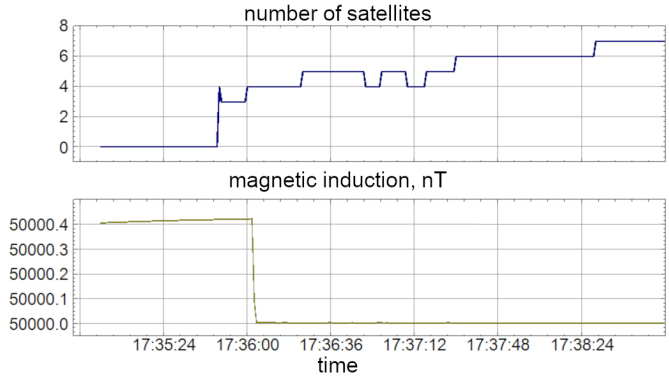

Fig. 2. Implementation of atomic clock correction. (top) Number of visible satellites used to calculate position and time, a minimum of 4 satellites is required for solution. (bottom) Estimation of magnetic induction (nT) after clock correction. The horizontal axis represents time.

The bottom graph in Fig. 2 represents the value of the field. The input is the constant frequency of 174,928.85 Hz, which corresponds to the induction value of 50,000 nT (Cesium). However, before 17:36:00 the value is incorrect, and we see an error of about 10^{-5}, or 0.4 nT. Moreover, the value changes by 0.02 nT or about $5 \cdot 10^{-7}$ in one minute due to warming up. Both of these numbers indicate the limited accuracy and stability of our 1 GHz counter. But when the PPS signal appears, the field estimate takes on the true value.

The presented experimental result practically proves the effectiveness of using the PPS signal.

V. Optimization of the Frequency Estimate

As we have already mentioned, information about the length of each wave covered by the sample gate can be used to estimate the Larmor frequency. Depending on which filter is applied, the value of the estimation error will be different. Let's try to formulate and solve an optimization problem to obtain the best estimate of the frequency $\tilde{f}_{Lf}$.

Each Larmor wave number i has its period estimate $\tilde{T}_i$, if we put $N = 1$ in (4). Our goal is to get an estimate for one sample. Assume that the real frequency f is the same for all waves. Then, adding several Larmor periods T_L and multiplying by f, we get the number of Larmor waves. For example,

$$\sum_{i=1}^{j} T_L f = j. \tag{8}$$

In our case $\tilde{T}_i \neq T_L$. To approximate (8) we can use the following form

$$\left(\sum_{i=1}^{j} \tilde{T}_i + t_0 \right) f \to j. \tag{9}$$

We need to add t_0, because the counting start time is almost always later than the start of the wave. This is clearly seen in Fig. 1, the plot of the measured signal.

Let's make the following notations in (9)

$$b = t_0 f, \quad t_j = \sum_{i=1}^{j} \tilde{T}_i.$$

Our goal is to find the unknowns b and f. The idea is to use the LSM for this. Then we can consider the following function and find its minimum:

$$J(f, b) = \sum_{j=1}^{N} \left(t_j f + b - j \right)^2 \to \min_{f,b}. \tag{10}$$

The minimum is obtained by solving the following system:

$$f \cdot \sum_{j=1}^{N} t_j^2 + b \cdot \sum_{j=1}^{N} t_j = \sum_{j=1}^{N} j t_j, \tag{11}$$

$$f \cdot \sum_{j=1}^{N} t_j + b \cdot N = \frac{N(N+1)}{2}. \tag{12}$$

Since we don't really need to know the value of b, let's express it from (12) and substitute it in (11). The frequency estimate can then be calculated as:

$$\tilde{f}_{Lf} = \frac{\sum_{j=1}^{N} \left(j - \frac{N+1}{2} \right) t_j}{\sum_{j=1}^{N} t_j^2 - \frac{1}{N} \left(\sum_{j=1}^{N} t_j \right)^2}. \tag{13}$$

Analyzing (13), we see that the numerator contains a digital filter [29], and if we group the pairs $t_N - t_{N/2}$, $t_{N-1} - t_{(N/2)-1}$ and so on, we will see that we are averaging $N/2$ Larmor period estimates. Each of them is evaluated at half of the sample gate. N is the total number of Larmor waves. But the analysis of the denominator is more difficult. According to the dimensional analysis, it contains an estimate of the squared Larmor period. It also uses all measured periods, but is difficult to analyze.

We can say for sure that the values of $\tilde{f}_{Lp}$ in (5) and $\tilde{f}_{Lf}$ in (13) are different. From the point of view of computational speed, we see the main advantage of (5). All we need to do in this case is to perform an integer sum every Larmor period and one floating point division for every output sample. Thus, in the case of the ^{133}Cs sensor at 1 kHz sample rate, a maximum of 0.35 million integer operations and 1 thousand floating point operations per second are performed. In the case (13) there are three additional sums and two multiplications for each Larmor period. This gives about 2 million integer operations and 2 thousand floating point operations per second.

We can simplify the calculations a little maintaining accuracy. Let us substitute t_j by $j/\tilde{f}_{Lf}$ in the denominator of (13). The error of such a substitution will be of the order of the squared frequency estimation error. Having the well-known formulas

$$\sum_{j=1}^{N} j = \frac{N(N+1)}{2}, \quad \sum_{j=1}^{N} j^2 = \frac{N(N+1)(2N+1)}{6}, \quad (14)$$

we get

$$\frac{1}{\tilde{f}_{Lf}} \approx \frac{12}{N^2-1} \sum_{j=1}^{N} \left(j - \frac{N+1}{2} \right) t_j. \quad (15)$$

Here we have only about 1 million integer operations and 1 thousand floating point operations per second. Equation (15) is used by the developers of PPM sensors [30], [31].

To understand the advantages of (13), we must examine estimation errors.

VI. Error Analysis

First, let's rewrite (5) in a form equivalent to (13):

$$\tilde{f}_{Lp} = \frac{N}{t_N}. \quad (16)$$

For both (13) and (16) we can use the following error definition:

$$t_j = (j + \delta_j) \cdot T_L, \quad \delta_j \in \left(-\frac{f_L}{f_{clck}}, \frac{f_L}{f_{clck}} \right). \quad (17)$$

Using (17) for $j = N$ in (16) after Taylor expansion neglecting $O(\delta_N^2)$, we get

$$\tilde{f}_{Lp} = f_L - \frac{f_L}{N} \delta_N. \quad (18)$$

Let's do the same for $\tilde{f}_{Lf}$ in (13). After all calculations, we get

$$\tilde{f}_{Lf} = f_L \cdot \frac{\frac{N^3-N}{12} + \sum_{j=1}^{N} \left[j - \frac{N+1}{2} \right] \delta_j}{\frac{N^3-N}{12} + 2\sum_{j=1}^{N} \left[j - \frac{N+1}{2} \right] \delta_j + O(\delta_j^2)}. \quad (19)$$

Here we have used (17), and formulas (14). After Taylor expansion and by neglecting of $O(\delta_j^2)$ from (19) we obtain

$$\tilde{f}_{Lf} = f_L - \frac{f_L}{N} \left[\frac{12}{N^2-1} \sum_{j=1}^{N} \left\{ \delta_j \cdot \left(j - \frac{N+1}{2} \right) \right\} \right], \quad (20)$$

and here we have the linear digital filter that we have already mentioned in the previous section. Note, that the first order error will be the same for equation (15).

The worst case for (18) we have already seen in (6). For (20) the situation is even worse. Consider the case when the estimate of the first $N/2$ periods has the minimum error, while for the second $N/2$ periods the error is maximum. Then the sum in (20) gives about $N^2/4$, which leads to

$$\delta f_{Lf} = \frac{\Delta f_L}{f_L} \in \left(-\frac{3f_s}{f_{clck}}, \frac{3f_s}{f_{clck}} \right). \quad (21)$$

However, it should not be concluded that the algorithm (13) is less accurate than (16). Note that the case presented above is highly unusual. To have such distributed errors, the field must be changing during the sample gate. But this contradicts the assumption of a constant field. Assume that the Larmor period is k/f_{clck}. Then the counter value for it will be either $[k]$ or $[k]+1$, $[\cdot]$ is meaning rounding down to the nearest integer. This means that the worst case for (20) is when, for example, the estimate of the first $N/2$ periods has zero error, and the error is maximum for the second $N/2$ periods. Then the sum in (20) gives about $N^2/8$, which leads to

$$\delta f_{Lf} = \frac{\Delta f_L}{f_L} \in \left(-\frac{3f_s}{2f_{clck}}, \frac{3f_s}{2f_{clck}} \right). \quad (22)$$

Now the main question is how often do we encounter such undesirable conditions. Consider a piecewise constant increasing field to ignore its changes during one sample gate.

For the case (16) we will always have the best estimate when $kf_L/N = f_{clck}$, $k \in \mathbb{N}$. To be more specific, for an OPM sensor with a $f_{clck} = 1$ GHz counter and a 1 kHz sample rate, we will have this situation every 0.05 nT near an induction value of 50,000 nT. But the worst values will be next to the best ones. If we slightly change the period, sooner or later for one of the samples we will get the counter value changed by one, or the frequency changed by $1/f_{clck}$. This is shown in the top graph in Fig. 3. The value of 50,000.037 nT is estimated with an error of 0, -0.031 or 0.02 nT, and the error in the estimate of 50,000.039 nT can reach 0.048 nT.

In the case of (13), to get the same poor value, we need the Larmor period to be a multiple of the reference clock period, i.e. $kf_L = f_{clck}$, $k \in \mathbb{N}$. For the same conditions we will have it only every 8.75 nT. It can be seen from the lower graph in Fig. 3 that the error of the frequency LSM exceeds the error of the period LSM only once in the interval of 8.75 nT. The value of 50,005.335 nT is estimated with zero error by both algorithms, and the error of the value of 50,005.337 nT can be 0.049 nT and 0.074 nT for (16) and (13), respectively.

But what do we get in the case of a noisy signal? Fig. 4 compares the estimation error in the case of an ideal Larmor wave and a noisy one. It shows an evaluation result near the value of 50,005.335 nT. The top graph shows the errors for an

ideal signal. We have ± 0.049 nT error by (16) and ± 0.074 nT by (13). Adding the signal noise about 0.5 pT/$\sqrt{\text{Hz}}$, we get ± 0.278 nT error by (16) and only ± 0.058 nT by (13). We can conclude, that randomization has made it much more difficult to get the wrong counter value. Additional statistics for the range of induction 50,000–50,020 nT are presented in Table I.

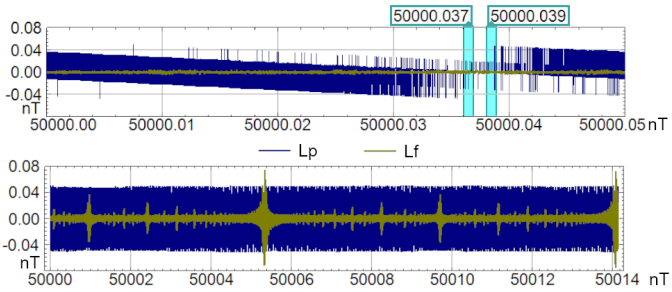

Fig. 3. Error in estimating magnetic induction (nT, vertical axis) depending on induction value (nT, horizontal axis) according to the algorithm (16) — dark blue line, Lp, and according to the algorithm (13) — dark yellow line, Lf. (top) The induction changes in the range 50,000.00–50,000.05 nT; zones of fixed input values of 50,000.037 nT and 50,000.039 nT are marked. (bottom) The induction changes in the range 50,000–50,014 nT.

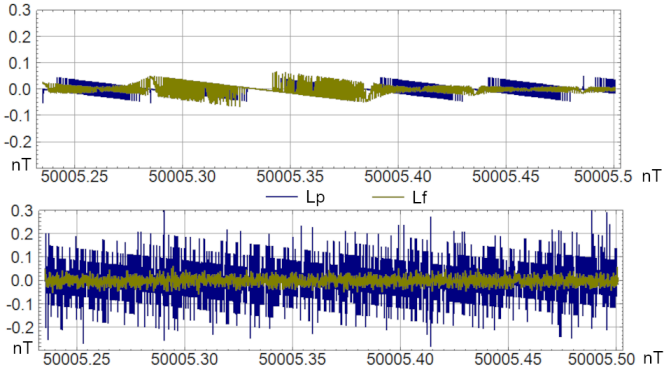

Fig. 4. Error in estimating magnetic induction (nT, vertical axis) depending on induction value (nT, horizontal axis) according to the algorithm (16) — dark blue line, Lp, and according to the algorithm (13) — dark yellow line, Lf in the range of 50005.25–50005.5 nT. (top) Ideal input signal, no noise. (bottom) Noisy input signal, Gaussian noise with spectral density 0.5 pT/$\sqrt{\text{Hz}}$.

Thus, even in the case of an ideal input signal, the sampling error for the presented LSM frequency estimate will in most cases be much smaller than for the LSM period estimate. With a real sensor, OPM or PPM, random noise will be added to the Larmor signal. If the Larmor period noise is comparable to $1/f_{clck}$, it will be effectively filtered by the algorithm (13). We can see that the peak-to-peak error range even improves for $\tilde{f}_{Lf}$, but not for $\tilde{f}_{Lp}$.

Discussing this result, we can say that in the case of the period estimation algorithm (5) the noise will appear in the same form as the δ error in the equation (18). The same can be said about the frequency estimation algorithm: the noise will be averaged using the filter (20). In the presence of Gaussian noise, the average of N independent implementations will always have a lower RMS than that of a single implementation. Moreover, in case of a constant input frequency, the frequency

TABLE I
INDUCTION ESTIMATION STATISTICS

value	$\tilde{f}_{Lp}$	$\tilde{f}_{Lf}$
ideal signal		
peak-to-peak	± 50 pT	± 74 pT
RMS	20 pT	4 pT
noisy signal		
peak-to-peak	± 285 pT	± 58 pT
RMS	91 pT	16 pT

estimation algorithm (13) is the best in terms of least squares error [32].

It turns out that it is quite natural to associate estimation errors with sensor noise. It can be seen from (6), (22) that the estimation error itself is directly proportional to the sampling frequency f_s. As for the sensor, if its noise is close to white noise, then its value will increase more slowly, proportional to $\sqrt{f_s}$. So we can find the intersection:

$$\sigma_B \cdot \sqrt{f_s} = B_0 \cdot \kappa \frac{f_s}{f_{clck}}, \tag{23}$$

where the left part represents the sensor noise with σ_B (nT/$\sqrt{\text{Hz}}$), while the right part is the root mean square error of estimation of the field induction value B_0 (nT) with κ as the scale factor depending on the algorithm.

From (23) we can obtain the maximum sampling rate that can be used without the estimation error exceeding the sensor noise:

$$f_{smax} = \frac{f_{clck}^2}{\kappa^2} \cdot \frac{\sigma_B^2}{B_0^2}, \tag{24}$$

having κ calculated from Table I for period estimation as $\kappa_p = 0.4$ and for frequency estimation as $\kappa_f = 0.08$. Please note that we have B_0^2 in the denominator, so it is better to calculate (24) for the largest induction value — 100,000 nT. The two functions for κ_p and κ_f are presented in fig. 5 in case of Scintrex CS-3 sensor with a noise of 0.6 pT/$\sqrt{\text{Hz}}$ [17].

VII. EXPERIMENTS

All results presented in this section are obtained using the least squares method for frequency estimation (13) and satellite clock correction. The first experiment was carried out with a 1 GHz counter of the GT-MAG series of the Russian company "Geotechnologies" [33]. The induction was estimated using the formula (13). We compared the noise of two Scintrex CS-3 [17] and one Radar-mms DM [19] sensors at a sampling rate of 1 kHz. Having similar characteristics, in practice they showed some differences.

All recordings were made far from any sources of industrial noise. However, as we see in Fig. 6, 7, there was a 50 Hz

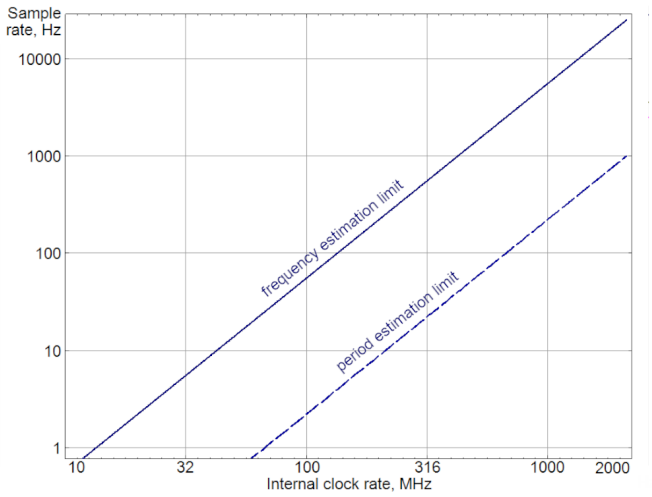

Fig. 5. The sample rate limits (Hz, vertical axis) for the period estimation algorithm (16) (dashed line) and for the frequency estimation algorithm (13) (solid line) as a function of the reference clock rate (MHz, horizontal axis) in the case of Scintrex CS3 sensor noise for the field induction value of 100,000 nT.

component. Fig. 6 shows a short interval in the time domain. The amplitude at 50 Hz is about 1 nT peak-to-peak. All sensors show very similar signals, except that the DM looks a bit noisier.

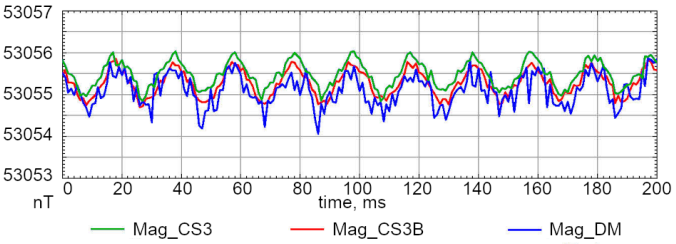

Fig. 6. Synchronous induction measurements in time domain (nT) as functions of samples, sample rate is 1 kHz: Mag_CS3 (green) and Mag_CS3B (red) — Scintrex CS-3 sensors, Mag_DM (blue) — Radar-mms DM sensor.

Fig. 7 shows the frequency domain representation. Recordings on the interval of 4096 ms were converted to the frequency domain using the FFT. In addition to the sensor noise, the effect of the 50 Hz frequency is noticeable on the odd harmonics (50, 150, 250, 350 Hz). The resulting curves additionally include an estimation error (the same for all three sensors). Having RMS of 4 pT at 1 kHz we get about 0.1 pT/$\sqrt{\text{Hz}}$, so we can ignore this value for both sensor types. For the CS-3 sensors (Sp_CS3 and Sp_CS3B) we see that the spectral density of the signals varies in the range of 0.2–2 pT/$\sqrt{\text{Hz}}$, with an average of 0.7 pT/$\sqrt{\text{Hz}}$. For the DM sensor (Sp_DM) it varies within 1–3 pT/$\sqrt{\text{Hz}}$, with an average of 2.6 pT/$\sqrt{\text{Hz}}$. Thus, for CS-3 the noise is about 0.6 pT/$\sqrt{\text{Hz}}$, and for the DM sensor it is at the level of 2.5 pT/$\sqrt{\text{Hz}}$.

Note that for both types of Cesium OPM sensors, the noise level is fairly flat in the presented frequency band. This means that we can indeed consider the sensor noise as white noise of the appropriate intensity, at least in this frequency band. This makes us more confident in applying the optimal frequency

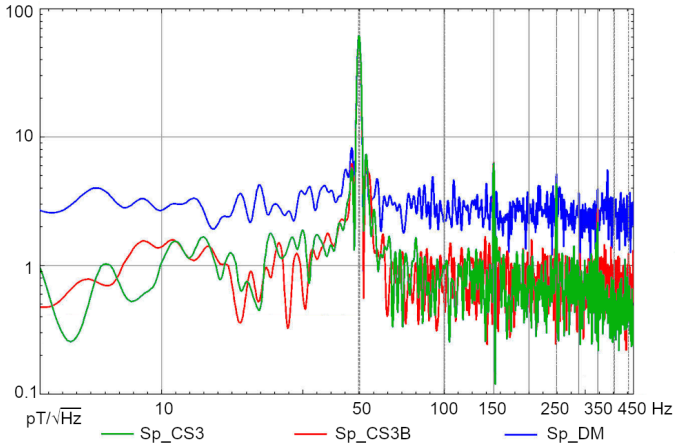

Fig. 7. Synchronous induction measurements in frequency domain, sample rate 1 kHz, accumulation for 4 s: Sp_CS3 (green) and Sp_CS3B (red) — Scintrex CS-3 sensors, Sp_DM (blue) — Radar-mms DM sensor.

estimation algorithm for such sensors.

The results of the second experiment are from an airborne survey where the same equipment — Scintrex CS-3 and GT-MAG counter — were used together with the EQUATOR EM system [34]. This system generates magnetic field pulses to induce currents in the ground and estimates subsurface conductivity using secondary field measurements. Each pulse has a half-sine shape, duration is about 1.9 ms. After a pause of about 4.5 ms, it is repeated in the opposite direction. Fig. 8 shows the moment when the EM system is turned on. We can see that the pulse amplitude is about 30 nT. Actually it is about 250 nT, but since the field vector of the EM system is not collinear with the vector of the Earth field, we can't see it in scalar measurements.

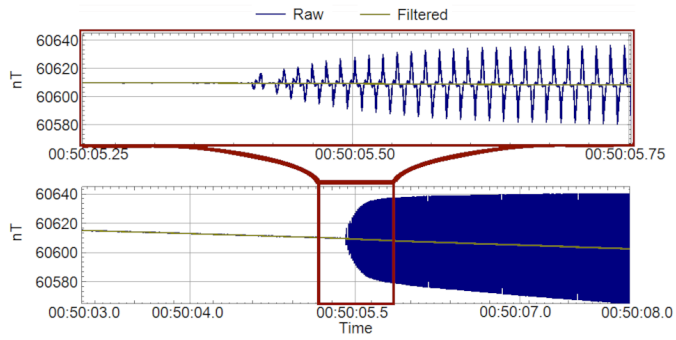

Fig. 8. In-flight induction measurements (nT) in the presence of an electromagnetic field source: raw signal sampled at 926 Hz (dark blue lines) and filtered signal output at 26 Hz (dark yellow line). (top) Time range 00:50:05.25–00:50:05.75, the moment the EM system is turned on. (bottom) Time range 00:50:03–00:50:08.

The question is whether, with such a rapidly changing field, up to 10^5 nT/s, the algorithm or the sensor itself will generate any additional noise. In this experiment, after measuring the induction at a sampling rate of 926 Hz, we independently averaged every three periods of the EM field (77 Hz) using a simple rectangular filter.

We can say that we successfully separate the low frequency and the high frequency parts of the magnetic field, since

TABLE II
FILTERING ALTERNATING FIELD

value	raw	filtered
EM field off		
peak-to-peak	±0.18 nT	±0.02 nT
RMS/$\sqrt{\text{Hz}}$	2.0 pT	2.2 pT
EM field on		
peak-to-peak	±47 nT	±0.02 nT
RMS/$\sqrt{\text{Hz}}$	760 pT	2.4 pT

the magnetic field noise for the filtered value remains approximately the same before and after turning on the EM field. Fig. 9 shows data for five minutes of flight, where the bottom graph is the non-normalized fourth difference of the filtered value. This parameter is usually analyzed to estimate aeromagnetic survey noise. The fourth difference is almost not affected by the moment the EM field is turned on. We have ±0.36 nT before the start and ±0.38 nT after it. This is consistent with the noise statistics presented in Table II. The noise before the appearance of the EM field is 2–3 pT/$\sqrt{\text{Hz}}$, both with and without filtering. It is four times the noise of the sensor because it is mounted on a moving platform. In the presence of the EM field, the noise of the filtered data is the same, and without filtering it is 760 pT/$\sqrt{\text{Hz}}$.

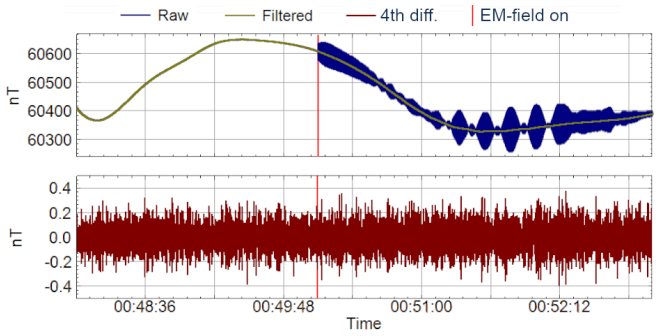

Fig. 9. In-flight induction measurements in the presence of an electromagnetic field source: the moment the EM system is turned on is marked with a red line; (top) raw signal sampled at 926 Hz (dark blue lines) and filtered signal output at 26 Hz (dark yellow line), nT; (bottom) fourth difference, not normalized, nT.

VIII. CONCLUSION

We have considered two algorithms, both based on LSM. One averages the periods over one sample, the other averages the frequency over the same time gate.

We have shown that in the case of an ideal input signal, for a ^{133}Cs OPM sensor and a 1GHz reference frequency at 1 kHz sampling rate there will be a frequency estimation error of ±0.074 nT that is 50% larger than a period estimation error of ±0.049 nT, but this occurs only at certain values of magnetic induction, approximately every 9 nT. In all other cases, it is much lower, about an order of magnitude.

In the case of a noisy signal, these poor values disappear as they need a very specific distribution of Larmor periods. As a result, frequency estimation always performs better than period estimation: the frequency estimation error of ±0.058 nT in the case of 0.5 pT/$\sqrt{\text{Hz}}$ noise is 5 times better than the period estimation error of ±0.278 nT under the same conditions. This is why it is necessary to analyze the relationship between sensor noise and estimation error. The maximum sample rate formula shows the dependence on the square of the reference clock frequency.

We have also described a way to ensure absolute measurement accuracy using GNSS signals. If the GNSS receiver has a PPS output, the uncertainty can be as low as $2 \cdot 10^{-8}$, or about 1 pT.

ACKNOWLEDGMENT

We would like to dedicate this study to the memory of two wonderful engineers, Victor Popovich and Vladimir Nazarenko, who made the best frequency counters we have ever had in airborne magnetics. Unfortunately, both of them are no longer with us.

We would also like to thank the Geotechnologies company for providing us with the equipment necessary for the experiment.

REFERENCES

[1] W. M. Telford, L. P. Geldart, and R. E. Sheriff, *Applied Geophysics,* 2nd ed., New York, NY, USA: Cambridge University Press, 2004.
[2] G. Noriega, "Aeromagnetic Compensation in Gradiometry — Performance, Model Stability, and Robustness," *IEEE Geoscience and Remote Sensing Letters*, vol. 12, no. 1, pp. 117–121, Jan. 2015, 10.1109/LGRS.2014.2328436.
[3] E. V. Karshakov, and M. V. Kharichkin, "A stochastic estimation problem at aeromagnetometer deviation compensation," *Automation and Remote Control*, 69, pp. 1162–1170, 2008, 10.1134/S0005117908070072.
[4] Y. Feng, Y. Zheng, L. Chen, X. Qu, and G. Fang. "Method of Eliminating Helicopter Vibration Interference Magnetic Field with a Pair of Magnetometers," *Applied Sciences*, 12, pp. 2065(1–15), 2022, 10.3390/app12042065.
[5] J. Moilanen, "Modern Methods of Airborne Electromagnetic Survey," *Izvestiya, Physics of the Solid Earth,* 58, pp. 755–764, 2022, 10.1134/S106935132205007X.
[6] A. A. Logachev, "The Development and Applications of Airborne Magnetometers in the U.S.S.R.," *Geophysics,* 11(2), pp. 135–147, 1946, 10.1190/1.1437230.
[7] P. Hood, "History of aeromagnetic surveying in Canada," *The Leading Edge*, 26(11), pp. 1384–1392, Nov. 2007, 10.1190/1.2805759.
[8] H. Liu, H. Dong, J. Ge, and B. Bai, "A High Precision Proton Magnetometer Based on a Multi-Channel Frequency Measurement," *2016 IEEE International Instrumentation and Measurement Technology Conference Proceedings*, Taipei, Taiwan, pp. 1–6, 2016, 10.1109/I2MTC.2016.7520474.
[9] N. Ma, S. Chen, and S. Zhang, "Proton magnetometer sensor design and its performance," *IOP Conf. Series: Earth and Environmental Science*, 734, pp. 012028, 2021, 10.1088/1755-1315/734/1/012028.
[10] H. Dong, S. Hu, J. Ge, H. Liu, W. Luo, Z. Yuan, J. Zhu, and H. Zhang, "A high-precision and fast-sampling frequency measurement method based on FPGA carry chain for airborne optically pumped cesium magnetometer," *Review of Scientific Instruments,* vol. 89, issue 7, pp. 075001-1–075001-7, Jul. 2018, 10.1063/1.5036822.
[11] L. Zhang, Y. Yang, N. Zhao, J. He, and J. Wang, "A Multi-Pass Optically Pumped Rubidium Atomic Magnetometer with Free Induction Decay," *Sensors*, 22, 7598, pp. 1–12, 2022, 10.3390/s22197598.

[12] N. Beverini, O. Faggioni, C. Carmisciano, E. Alzetta, E. Maccioni, M. Francesconi, A. Donati, E. Simeone, and F. Strumia, "A project for a new alkali vapor magnetometer, optically pumped by a diode laser," *Annali di Geofisica*, vol. 40, no. 3, pp. 227–432, Aug. 1998, 10.4401/ag-4335.
[13] A. K. Vershovskii, and A. S. Pazgalev, "Optically Pumped Quantum MX Magnetometers: Digital Measurement of the MX Resonance Frequency in a Rapidly Varying Field," *Technical Physics*, vol. 51, no. 7, pp. 924–928, 2006, 10.1134/S1063784206070188.
[14] A. K. Vershovskii, and A. S. Pazgalev, "Optically Pumped Quantum Magnetometer Employing Two Components of Magnetic Moment Precession Signal," *Technical Physics Letters*, vol. 37, no. 1, pp. 23–26, 2011, 10.1134/S106378501101007X.
[15] J. D. Fairhead, G.R.J. Cooper, and S. Sander, "Advances in Airborne Gravity and Magnetics," *Proceedings of Exploration 17: Sixth Decennial International Conference on Mineral Exploration*, Toronto, Canada, pp. 113–127, Oct. 2017.
[16] A. J. Canciani, "Magnetic Navigation on an F-16 Aircraft using Online Calibration," *IEEE Transactions on Aerospace and Electronic Systems,* vol. 58, no. 1, pp. 420–434, Feb. 2022, 10.1109/TAES.2021.3101567.
[17] Scintrex CS-3 High Sensitivity Cs Magnetometer Sensor [Online]. Available: https://www.scintrexltd.com/product/cs-3-high-resolution-cesium-magnetometer-copy
[18] Geometrics G-824A Magnetometer [Online]. Available: https://www.geometrics.com/product/g-824a
[19] Radar-mms Magnetometer sensor DM [Online]. Available (in Russian): https://radar-mms.com/product/magnitometricheskie-sistemy/kvantovyy-geofizicheskiy-magnitometr
[20] S. Hu, H. Dong, J. Ge, and W. Luo, "A high-speed, continuous and no-intermittent frequency measurement algorithm for cesium optically pumped magnetometer," *2017 First International Conference on Electronics Instrumentation & Information Systems (EIIS),* Harbin, China, pp. 1–5, 2017, 10.1109/EIIS.2017.8298585.
[21] H. Dong, H. Liu, J. Ge, Z. Yuan, and Z. Zhao, "A High-Precision Frequency Measurement Algorithm for FID Signal of Proton Magnetometer," *IEEE Transactions on Instrumentation and Measurement,* vol. 65, no. 4, pp. 898–904, Apr. 2016, 10.1109/TIM.2016.2516299.
[22] Y. Peng, J. Ge, S. Zhou, H. Dong, and H. Liu, "A frequency-measurement technology of larmor precession signal in overhauser magnetometer based on spectrum zoom algorithm," *ICIC Express Letters, Part B: Applications,* vol. 6, pp. 2635–2642, Sep. 2015.
[23] Y. Xu, H. Yi, W. Zhang, and H. Xu, "An Improved CZT Algorithm for High-Precision Frequency Estimation," *Applied Sciences*, 13, 1907, 2023, 10.3390/app13031907.
[24] J. Ge, X. Qiu, H. Dong, W. Luo, H. Liu, Z. Yuan, J. Zhu, and H. Zhang, "Short-Time and High-Precision Measurement Method for Larmor Frequency of Marine Overhauser Sensor," *IEEE Sensors Journal,* vol. 18, no. 4, pp. 1442–1448, Feb. 2018, 0.1109/JSEN.2017.2785381
[25] S. Fan, S. Chen, S. Zhang, X. Guo, and Q. Cao, "An improved Overhauser magnetometer for Earth's magnetic field observation," *Proc. SPIE 9972, Earth Observing Systems XXI,* 99721N (19 September 2016), 10.1117/12.2235522.
[26] O. H. Schmitt, "A Thermionic Trigger," *Journal of Scientific Instruments,* vol. 15, pp. 24–26, 1938, 10.1088/0950-7671/15/1/305
[27] M. S. Grewal, L. R. Weill, A. P. Andrews, *Global Positioning Systems, Inertial Navigation, and Integration,* NY, New York, USA: John Wiley & Sons, Inc., 2001.
[28] O. N. Pardo-Zamora, R. d. J. Romero-Troncoso, J. R. Millan-Almaraz, D. Morinigo-Sotelo, R.A. Osornio-Rios, and J.A. Antonino-Daviu, "Power Quality Disturbance Tracking Based on a Proprietary FPGA Sensor with GPS Synchronization," *Sensors,* 21, pp. 3910-1–3910-21, 2021, 10.3390/s21113910.
[29] R. W. Hamming, *Digital Filters,* 3rd ed., Englewood Cliffs, New Jersey, USA: Prentice-Hall, 1998.
[30] A.Y. Denisov, V.A. Sapunov, and B. Rubinstein. "Broadband mode in proton-precession magnetometers with signal processing regression methods," *Measurement Science and Technology*, 25, pp. 055103(1–6), 2014, 10.1088/0957-0233/25/5/055103.
[31] G.P. Hancke. "The optimal frequency estimation of a noisy sinusoidal signal," *IEEE Transactions on Instrumentation and Measurement*, 39(6), pp. 843–846, 1990, 10.1109/19.65780.
[32] D. Simon, *Optimal State Estimation: Kalman, H∞, and Nonlinear Approaches,* New Jersey, USA: John Wiley & Sons, Inc., 2006.
[33] Geotechnologies Magnetometers GT-MAG [Online]. Available: https://www.geotechnologies-rus.com/eng/gt-mag.php
[34] E. V. Karshakov, Y. G. Podmogov, V. M. Kertsman, and J. Moilanen, "Combined Frequency Domain and Time Domain Airborne Data for Environmental and Engineering Challenges," *Journal of Environmental and Engineering Geophysics,* vol. 22, no. 1, pp. 1–11, Mar. 2017, 10.2113/JEEG22.1.1

Evgeny V. Karshakov was born in Penza city, USSR, in 1976. He received the specialist degree in mechanics and applied mathematics from the Moscow State University, in 1998 and the Ph.D. degree in physics and mathematics from the same University. In 2019 he received D.Sc. degree in technical sciences from the Institute of Control Sciences of Russian Academy of Sciences.

From 2005 until now he is with the Dynamic Control Systems Laboratory of the Institute of Control Sciences of Russian Academy of Sciences, Moscow, Russia. Since 2018 he is the head of the Laboratory. His research interests are geophysics (magnetics, electromagnetics, gravity), navigation (inertial, satellite, field-aided), control systems.

Andrey K. Volkovitsky was born in Moscow city, USSR, in 1955. He received the specialist degree in engineering from the Moscow Institute of Electronic Machine Building, in 1981, the Ph.D. degree in technical sciences from the Institute of Control Sciences of Russian Academy of Sciences in 2012. In 2022 he received D.Sc. degree in technical sciences from the Institute of Control Sciences of Russian Academy of Sciences.

From 2005 until now he is with the Dynamic Control Systems Laboratory of the Institute of Control Sciences of Russian Academy of Sciences, Moscow, Russia. Many years he was a leading researcher of the Laboratory. His research interests include airborne geophysics (magnetics, electromagnetics, gamma-ray, infrared scanning etc) and geophysical equipment.